

1 *Supplement of*

2 **Winter brown carbon over six China's megacities: Light**
3 **absorption, molecular characterization, and improved**
4 **source apportionment revealed by multilayer perceptron**
5 **neural network**

6 Diwei Wang¹, Zhenxing Shen^{1*}, Qian Zhang², Yali Lei³, Tian Zhang¹, Shasha Huang¹,
7 Jian Sun¹, Hongmei Xu¹, Junji Cao⁴

8 ¹Department of Environmental Science and Engineering, Xi'an Jiaotong University, Xi'an 710049,
9 China

10 ²Key Laboratory of Northwest Resource, Environment and Ecology, MOE, Xi'an University of
11 Architecture and Technology, Xi'an 710055, China

12 ³Key Lab of Geographic Information Science of the Ministry of Education, School of Geographic
13 Sciences, East China Normal University, Shanghai 200241, China

14 ⁴Key Lab of Aerosol Chemistry & Physics, SKLLQG, Institute of Earth Environment, Chinese Academy
15 of Sciences, Xi'an, China

16 *Correspondence to:* Zhenxing Shen (zxshen@mail.xjtu.edu.cn)

17

18 **Contents:**

19 **Text S1.** Optical properties of brown carbon (BrC) calculation

20 **Text S2.** The ANN-MLP model construction

21 **Table S1.** Information of sampling sites

22 **Table S2.** Concentrations of PM_{2.5} and carbonaceous components in six Chinese cities

23 **Figure S1.** The MLP neural network architecture used in this study

24 **Figure S2.** The relationship between the abundance of POC & SOC and BrC $b_{\text{abs}365}$ in six cities.

25 **Figure S3.** The relationship between the abundance of K⁺ and BrC $b_{\text{abs}365}$ in BJ, HrB, XA and WH.

26 **Figure S4.** Source profiles (bars and left y-axis) and percentage contributions (dots and y-axis) of each
27 chemical component resolved from PMF model analysis in six megacities.

28 **Figure S5.** Average source contribution to aerosol mass concentration that is estimated by PMF source
29 factor.

30 **Figure S6.** The correlation of the observed and modelled BrC $b_{\text{abs}365}$ for the six cities using MLP analysis.

31 **Text S1.** Optical properties of brown carbon (BrC) calculation

32 The light absorption coefficient (b_{abs} , Mm^{-1}) of the BrC was calculated using the following Eq. (S1):

33
$$b_{\text{abs}\lambda} = (A_{\lambda} - A_{700}) \times (V_{\text{ext}} \times \text{Portions}) \times \ln(10) / (V_{\text{aero}} \times L) \quad (\text{S1})$$

34 where A_{λ} and A_{700} represent the measured absorbance at a specified λ value and at 700 nm, respectively.

35 In this study, λ was set to 365 nm. Furthermore, V_{ext} represents the volume of the solvent extract (5 mL)

36 in which different portions of the filter were used to extract and estimate the absorption signal for the full

37 filter. Finally, V_{aero} represents the sampling volume, and L represents the path length of the cell (100 cm).

38 In this study, ambient OC was used to replace methanol-soluble OC (MSOC) because several studies

39 have indicated that most OC (~95%) can be extracted using methanol (Cheng et al., 2016; Huang et al.,

40 2018). The mass absorption efficiency (MAE, $\text{m}^2 \text{g}^{-1}$) of the filter extracts at λ was calculated using the

41 following Eq. (S2):

42
$$\text{MAE}_{\lambda} = b_{\text{abs}\lambda} / \text{OC} \quad (\text{S2})$$

43 The wavelength dependence of light absorption by BrC in the solvent extracts was derived using the

44 following Eq. (S3):

45
$$b_{\text{abs}\lambda} = K \times \lambda^{-\text{AAE}} \quad (\text{S3})$$

46 where K denotes a constant, λ denotes the wavelength of BrC, and AAE denotes the absorption Ångström

47 exponent. In this study, to avoid interference from inorganic species, AAE was calculated through the

48 linear regression fitting of $\log b_{\text{abs}}$ versus $\log \lambda$ in the 330–550-nm wavelength range.

49

50 **Text S2.** The ANN-MLP model construction

51 As shown in Figure S1, the ANN-MLP model includes three main layers: input layer, hidden layer,

52 and output layer. The two adjacent layers are fully connected (i.e., any neuron in the layer has connections

53 to all the neurons in the layer below). The input layer receives the daily contributions of the $\text{PM}_{2.5}$ sources

54 obtained from the PMF, and the BrC $b_{\text{abs}365}$ of six cities is set as the response variables in the output layer

55 gives. In this study, we limited only a one hidden layer was used to design MLP models to explore the

56 applicability of non-linear models. The neurons in the hidden layer computes the input data, realizes the

57 nonlinear mapping of the input information, and passes the information to the output layer. The number

58 of neurons in the hidden layer was determined automatically by the estimation algorithm (Borlaza et al.,

59 2021). The important parameters of neural network are the connection weights, bias and activation

60 functions between different layers. The weight represents the connection strength between neurons, and

61 the bias ensures that the output value calculated through the input cannot be activated randomly. The
62 activation function plays a role of nonlinear mapping, which can limit the output amplitude of neurons
63 within a certain range. The process of finding optimal parameters is the training process of neural network.
64 For instance, the transformation of the data from the input layer in the hidden layer can be expressed by
65 Eq. (S4):

$$66 \quad \forall j \in \{1, \dots, l\}, a_j = H\left(\sum_{i=1}^d w_{i,j}^G \times x_i + w_{0,j}^G\right) \quad (S4)$$

67 with $w_{i,j}^G$ the weight of the neuron between the input and hidden layer and $w_{0,j}^G$ an activation constant
68 for neuron j . The activation function H is often non-linear (Borlaza et al., 2021).

69 The feedforward ANN-MLP model was trained with a back-propagation process (Chang et al.,
70 2019). For training the ANN and obtaining the optimal model, the following treatments were developed:

71 (a) the dataset was standardized by subtracting the mean of the observed values and dividing by the
72 standard deviation, then the standardized values were saved as variable;

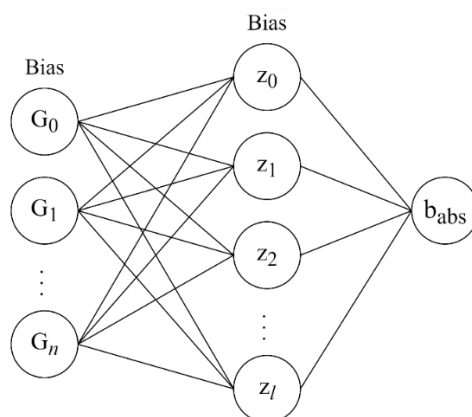
73 (b) 70% of the dataset was used as training set to train the model, and 30% of the dataset was used as test
74 set to monitor errors during training process;

75 (c) The nonlinear functions (activation functions) of sigmoid and hyperbolic tangent (TanH) were
76 introduced to perform nonlinear transformation on hidden variables, and then serve as the input of the
77 next fully connected layer;

78 (d) initialized randomly the weights of adjacent layer nodes, and then the scaled conjugate and stochastic
79 gradient descent optimization algorithms were used for iterative training to find the optimal weights
80 between nodes of each layer;

81 (e) the MLP training stops when the model output error reaches the set error standard.

82



input layer hidden layer output layer

83

84 **Figure S1. The MLP neural network architecture used in this study, where n is the number of PM_{2.5} sources**
 85 **from PMF, G is the daily standardized contribution of sources, and b_{abs} is the light absorption coefficient of**
 86 **BrC.**

87

Table S1. Information of sampling sites

Observation megacity	Location	Geographical China	Site description
Beijing	39.97° N, 116.36° E	North China	~8 m above ground level, in the north part of Beijing, which is close to several major roads including a highway and is surrounded by residences and restaurants.
Harbin	45.74° N, 126.73° E		~18 m above ground level, in the east of Harbin, surrounded by campus, roads, residential commercial emission sources
Xi'an	34.23° N, 108.88° E		~15 m above ground level, in the southeast of downtown Xi'an, surrounded by two lane roads, residential commercial districts.
Chengdu	30.70° N, 104.06° E	South China	~18 m above ground level, on the rooftop of a building of Southwest Jiaotong University, surrounded by commercial and residential areas and close to a train station
Guangzhou	23.12° N, 113.35° E		~30 m above ground level, in the central of Guangzhou, there is no obvious industrial pollution source near the monitoring station.
Wuhan	30.53° N, 114.39° E		~18 m above ground level, in the southeast of Wuhan city, surrounded by roads, residential commercial districts, this is a typical urban site with no industrial emission sources nearby.

88

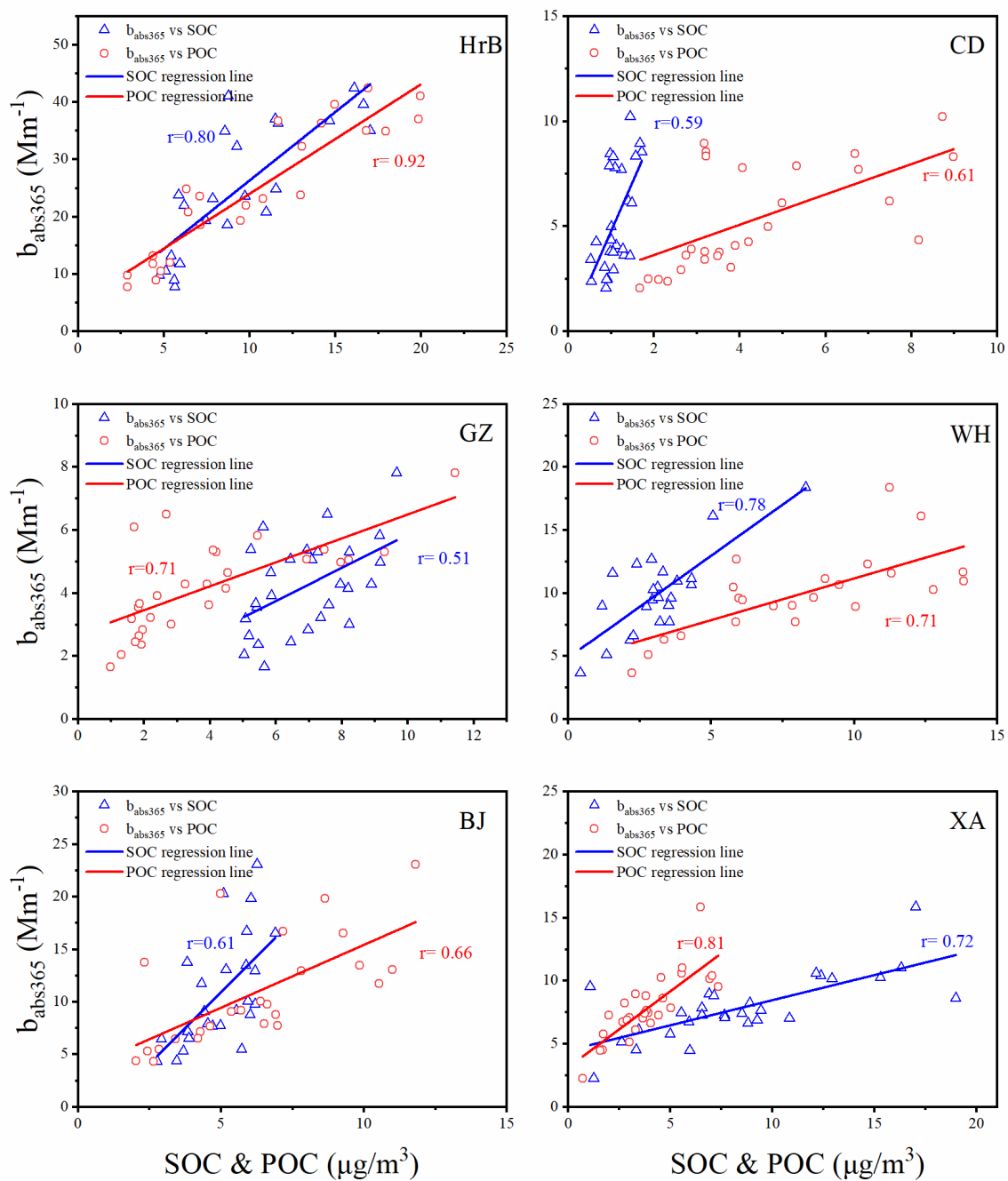
89 **Table S2. Concentrations of PM_{2.5} and carbonaceous components in six Chinese cities**

sites	PM _{2.5} ($\mu\text{g}\cdot\text{m}^{-3}$)	OC($\mu\text{g}\cdot\text{m}^{-3}$)	EC($\mu\text{g}\cdot\text{m}^{-3}$)	SOC($\mu\text{g}\cdot\text{m}^{-3}$)	POC($\mu\text{g}\cdot\text{m}^{-3}$)
Beijing	55.5 ± 41.5	12.5 ± 5.9	2.1 ± 1.7	5.0 ± 1.2	6.3 ± 2.9
Harbin	85.5 ± 43.9	19.4 ± 8.5	7.5 ± 5.6	9.2 ± 3.9	10.2 ± 5.5
Xi'an	80.7 ± 49.8	15.5 ± 7.9	3.6 ± 2.9	6.9 ± 3.8	7.8 ± 2.8

Chengdu	71.8 ± 28.2	5.6 ± 2.7	2.3 ± 1.0	1.0 ± 0.4	4.6 ± 2.2
Guangzhou	42.5 ± 17.2	10.9 ± 3.7	2.8 ± 2.0	6.9 ± 1.4	4.0 ± 2.7
Wuhan	63.9 ± 26.1	11.7 ± 4.8	4.2 ± 2.0	3.1 ± 1.6	8.2 ± 3.5

90

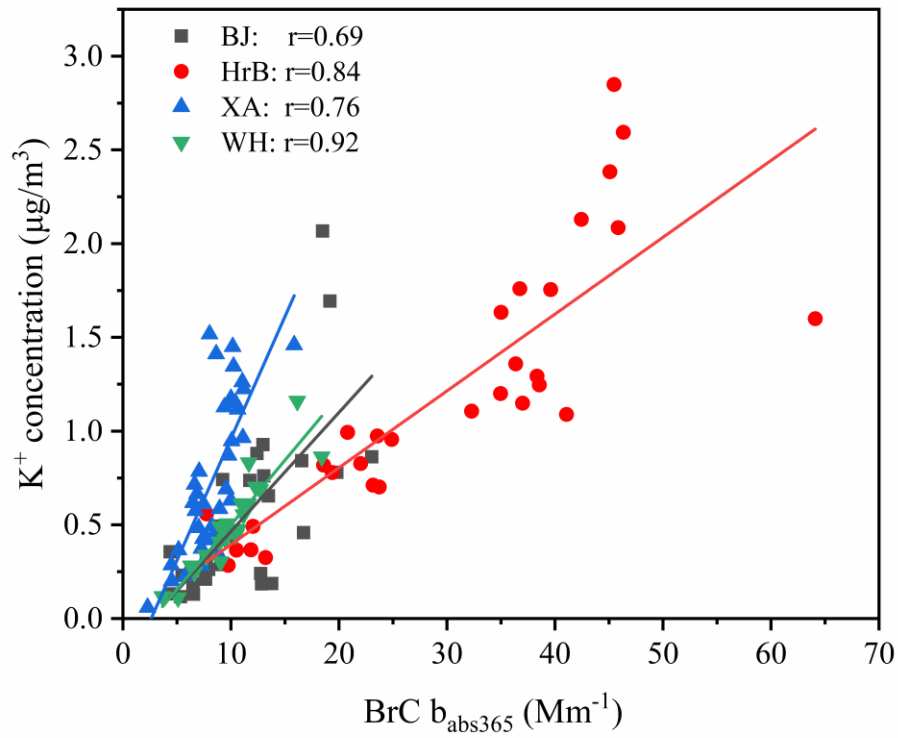
91



92

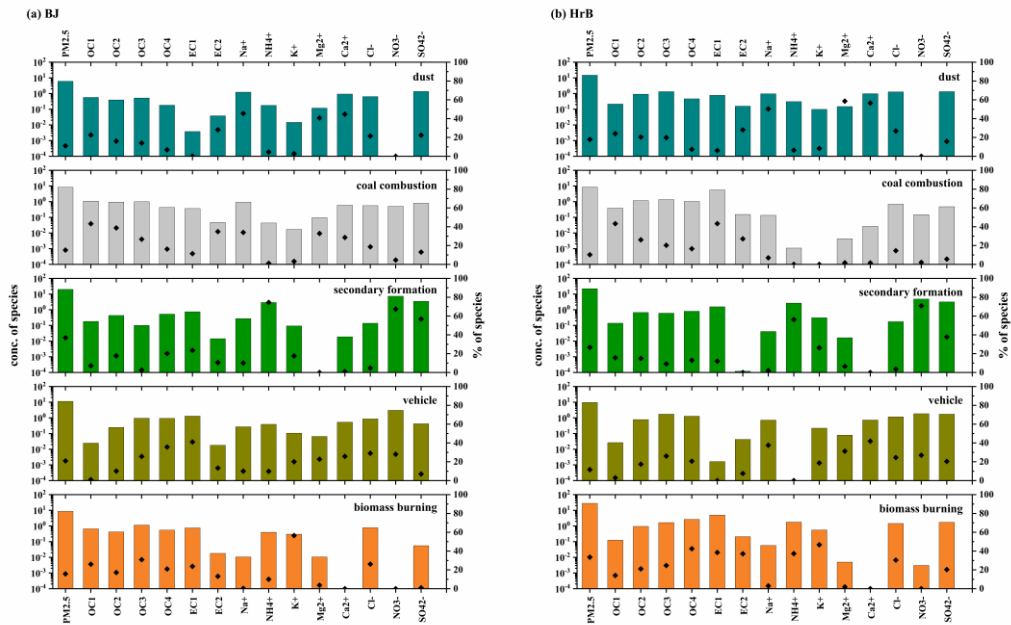
93

Figure S2. The relationship between the abundance of POC & SOC and BrC $b_{\text{abs}365}$ in six cities.

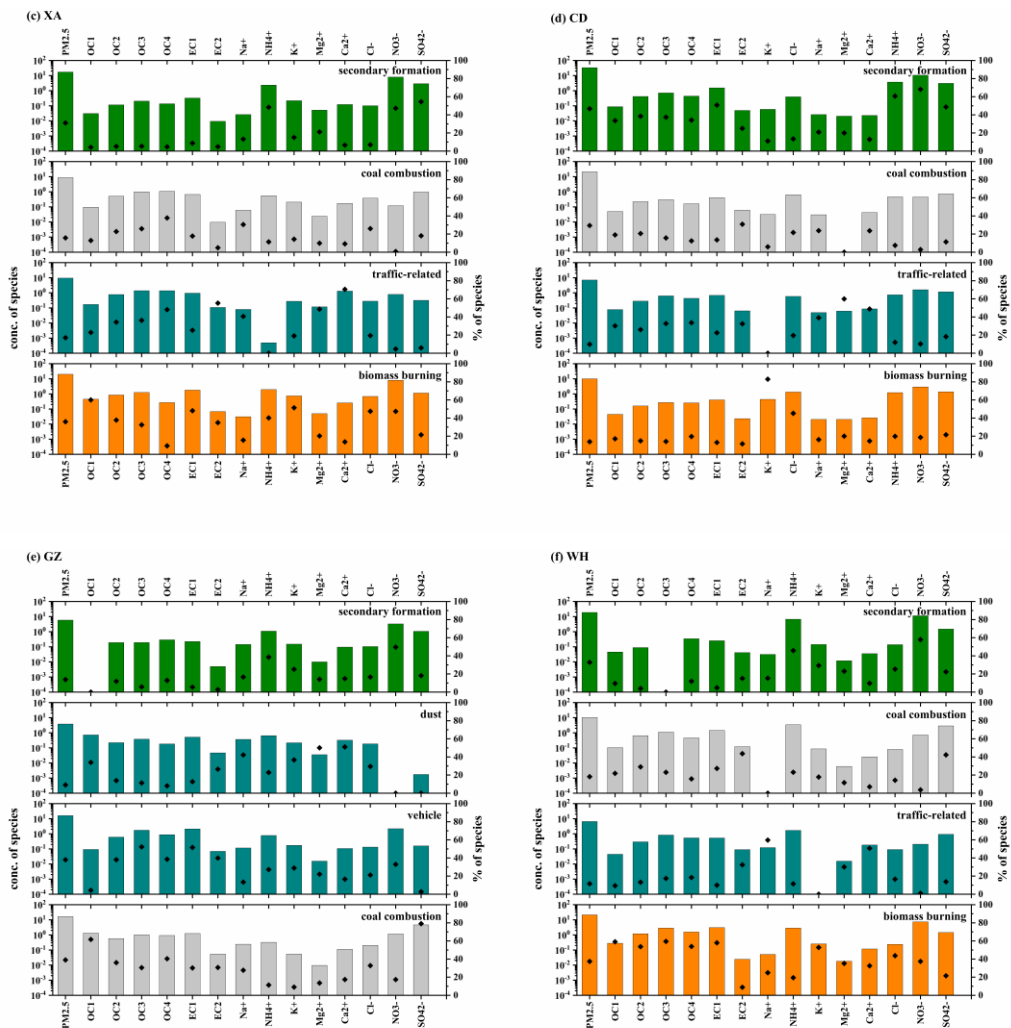


94

95 Figure S3. The relationship between the abundance of K^+ and $BrC\ b_{abs365}$ in BJ, HrB, XA and WH.



96



97

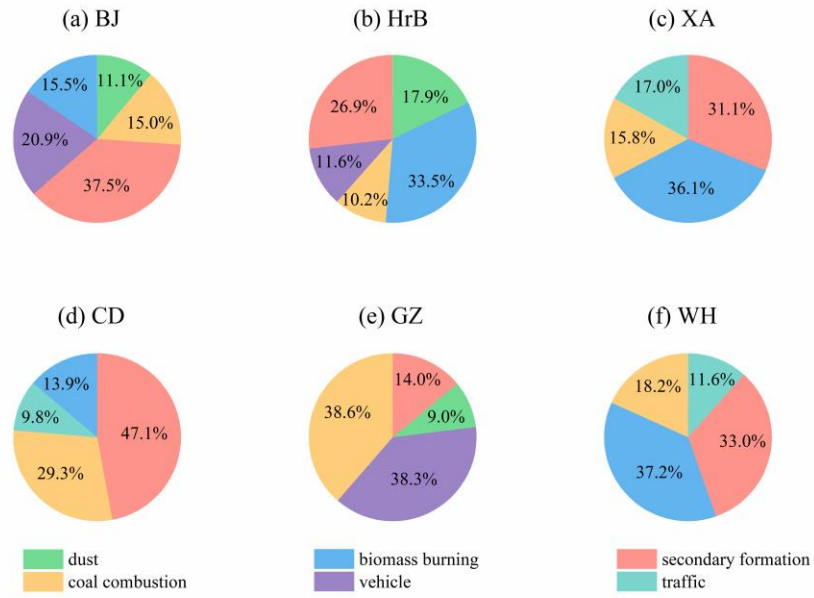
98

99

100

Figure S4. Source profiles (bars and left y-axis) and percentage contributions (dots and y-axis) of each chemical component resolved from PMF model analysis in six megacities.

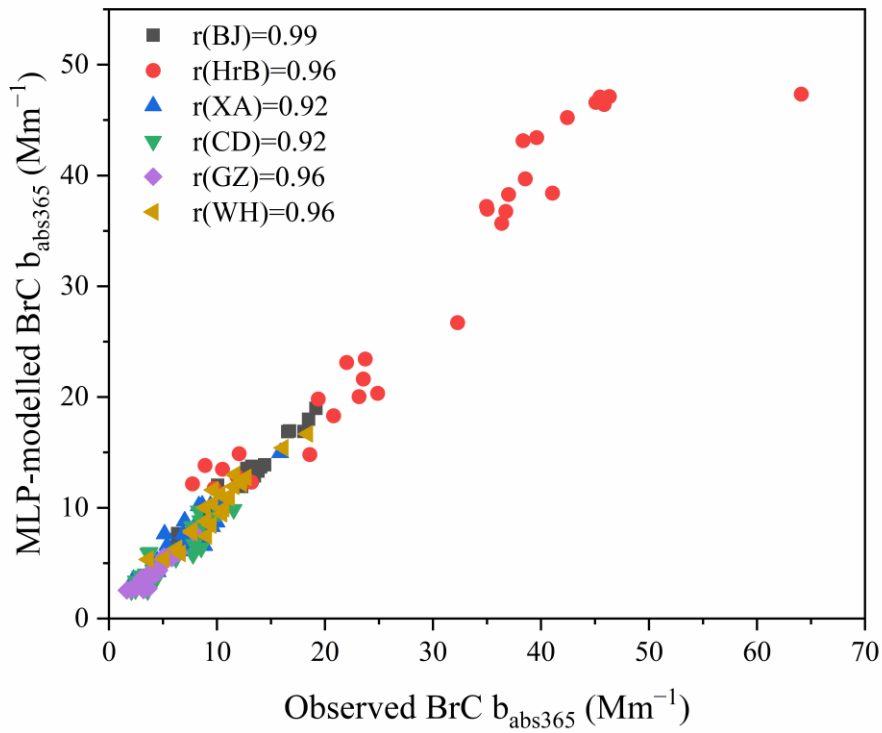
101



102

103

Figure S5. Average source contribution to aerosol mass concentration that is estimated by PMF source factor.



104

105

Figure S6. The correlation of the observed and modelled BrC b_{365} for the six cities using MLP analysis.

106

107 **Reference**

- 108 Borlaza, L. J. S., Weber, S., Jaffrezo, J.-L., Houdier, S., Slama, R., Rieux, C., Albinet, A., Micallef, S.,
109 Trébluchon, C., and Uzu, G.: Disparities in particulate matter (PM₁₀) origins and oxidative potential at a
110 city scale (Grenoble, France) – Part 2: Sources of PM₁₀ oxidative potential using multiple linear
111 regression analysis and the predictive applicability of multilayer perceptron neural network analysis,
112 *Atmos. Chem. Phys.*, 21, 9719-9739, <https://doi.org/10.5194/acp-21-9719-2021>, 2021.
- 113 Chang, T., Lu, J., Shen, Z., Huang, Y., Lu, D., Wang, X., Cao, J., and Morent, R.: Simulation and
114 optimization of the post plasma-catalytic system for toluene degradation by a hybrid ANN and NSGA-
115 II method, *Applied Catalysis B: Environmental*, 244, 107-119,
116 <https://doi.org/10.1016/j.apcatb.2018.11.025>, 2019.
- 117 Cheng, Y., He, K. B., Du, Z. Y., Engling, G., Liu, J. M., Ma, Y. L., Zheng, M., and Weber, R. J.: The
118 characteristics of brown carbon aerosol during winter in Beijing, *Atmos. Environ.*, 127, 355-364,
119 <https://doi.org/10.1016/j.atmosenv.2015.12.035>, 2016.
- 120 Huang, R. J., Yang, L., Cao, J., Chen, Y., Chen, Q., Li, Y., Duan, J., Zhu, C., Dai, W., Wang, K., Lin, C.,
121 Ni, H., Corbin, J. C., Wu, Y., Zhang, R., Tie, X., Hoffmann, T., O'Dowd, C., and Dusek, U.: Brown
122 Carbon Aerosol in Urban Xi'an, Northwest China: The composition and light absorption properties,
123 *Environ. Sci. Technol.*, 52, 6825-6833, <https://doi.org/10.1021/acs.est.8b02386>, 2018.